

Article

Discovery of “Meteoritic” Layered Disulphides $ACrS_2$ ($A = Na, Cu, Ag$) in Terrestrial Rock

Evgeny V. Galuskin ^{1,*}, Irina O. Galuskina ¹, Yevgeny Vapnik ² and Grzegorz Zieliński ³¹ Faculty of Natural Sciences, Institute of Earth Sciences, University of Silesia, 41-200 Sosnowiec, Poland² Department of Geological and Environmental Sciences, Ben-Gurion University of the Negev, P.O. Box 653, Beer-Sheva 84105, Israel³ Polish Geological Institute—National Research Institute, Rakowiecka 4, 00-975 Warsaw, Poland

* Correspondence: evgeny.galuskin@us.edu.pl

Abstract: For the first time, chromium disulphides, known from meteorites, such as caswellsilverite, $NaCrS_2$; grokhovskiyite, $CuCrS_2$; and a potentially new mineral, $AgCrS_2$, as well as the products of their alteration, such as schöllhornite, $Na_{0.3}CrS_2 \cdot H_2O$, and a potentially new mineral with the formula $\{Fe_{0.3}(Ba,Ca)_{0.2}\}CrS_2 \cdot 0.5H_2O$, have been found in terrestrial rock. Layered chromium disulphides were found in unusual phosphide-bearing breccia of the pyrometamorphic Hatrurim Complex in the Negev Desert, Israel. The chromium disulphides belong to the central fragment of porous gehlenite paralava cementing altered host rock clasts. The empirical formula of caswellsilverite is $(Na_{0.77}Sr_{0.03}Ca_{0.01})_{\Sigma 0.81}(Cr^{3+}_{0.79}Cr^{4+}_{0.18}V^{3+}_{0.01}Fe^{3+}_{0.01})_{\Sigma 0.99}S_2 \cdot 0.1H_2O$, and the end-member content of $NaCrS_2$ is 76%. It forms single crystals in altered pyrrhotite aggregates. Grokhovskiyite has the empirical formula $\{Cu^{+}_{0.84}Fe^{3+}_{0.10}Ca_{0.06}Na_{0.01}Sr_{0.01}Ba_{0.01}\}_{\Sigma 1.03}(Cr^{3+}_{0.94}Fe^{3+}_{0.05}V^{3+}_{0.05})_{\Sigma 1.00}S_2 \cdot 0.35H_2O$, and the $CuCrS_2$ end-member content is 75–80%. A potentially new Ag-bearing chromium disulphide is characterised by the composition $(Ag_{0.89}Cu_{0.07})_{\Sigma 0.96}(Cr_{0.98}Fe_{0.03}V_{0.01}Ni_{0.01})_{\Sigma 1.04}S_2$. Caswellsilverite, grokhovskiyite and $AgCrS_2$ form in gehlenite paralava at high temperatures (near 1000 °C) and low pressure under reducing conditions. The structure of the layered chromium disulphides, $MCrS_2$, is characterised by the presence of hexagonal octahedral layers $(CrS_2)^{1-}$, between which M-sites of the monovalent cations Ag, Cu and Na set. A low-temperature alteration of the layered chromium disulphides, when schöllhornite and $\{Fe_{0.3}(Ba,Ca)_{0.2}\}CrS_2 \cdot 0.5H_2O$ form, is reflected in the composition and structural modification of the layer with monovalent cations, whereas the octahedral layer $(CrS_2)^{1-}$ remains unchanged.

Keywords: layered chromium disulfides; caswellsilverite; grokhovskiyite; schöllhornite; composition; Raman; Hatrurim Complex; Israel



Citation: Galuskin, E.V.; Galuskina, I.O.; Vapnik, Y.; Zieliński, G. Discovery of “Meteoritic” Layered Disulphides $ACrS_2$ ($A = Na, Cu, Ag$) in Terrestrial Rock. *Minerals* **2023**, *13*, 381. <https://doi.org/10.3390/min13030381>

Academic Editor: Roman Skála

Received: 14 February 2023

Revised: 1 March 2023

Accepted: 7 March 2023

Published: 9 March 2023



Copyright: © 2023 by the authors. Licensee MDPI, Basel, Switzerland. This article is an open access article distributed under the terms and conditions of the Creative Commons Attribution (CC BY) license (<https://creativecommons.org/licenses/by/4.0/>).

1. Introduction

In the unusual phosphide-bearing breccia of the pyrometamorphic Hatrurim Complex, discovered in 2019 in the Negev Desert, Israel [1], numerous crystals of caswellsilverite, $NaCrS_2$, rare grains of grokhovskiyite and a potentially new mineral, $AgCrS_2$, as well as products of their alteration—schöllhornite, $Na_{0.3}CrS_2 \cdot H_2O$ —and a potentially new mineral with the simplified formula $\{Fe_{0.3}(Ba,Ca)_{0.2}\}CrS_2 \cdot 0.5H_2O$ (thereafter referred to as “mineral X”), were detected.

Caswellsilverite was first described in Norton County enstatite achondrite (aubrite), Kansas, USA [2]. Later it was found in enstatite chondrites in Qingzhen, Guiyang, Guizhou, China [3] and Yamato 691, Eastern Antarctica [4]; and in Northwest Africa 5217 [5] and Peña Blanca Springs (USA) aubrites [6]. It has also been found in some other meteorites [4]. Al Goresy et al. [7] found copper-bearing caswellsilverite and cation-deficit phase with the composition $(Cu_{0.35}Na_{0.32}Zn_{0.01})_{\Sigma 0.68}(Cr_{0.98}Fe_{0.05})_{\Sigma 1.03}S_2$ in enstatite chondrites (Yamato 691 and Qingzhen). A Cu-analogue of caswellsilverite, grokhovskiyite, has recently been

discovered in Uakit (IIAB) iron meteorite, Buryatia [8,9], and was almost simultaneously described in an iron meteorite from Arnhem Land, Northern Territory, Australia [10]. A mineral with the composition AgCrS_2 was detected in Peña Blanca Springs aubrites, USA, but its structure has not been investigated [11]. Caswellsilverite and grokhovskiyite in meteorites are, as a rule, associated with daubréelite, FeCr_2S_4 , and troilite or pyrrhotite. Caswellsilverite is easily hydrated and transforms into schöllhornite, $\text{Na}_{0.3}\text{CrS}_2 \cdot \text{H}_2\text{O}$ [12], cronusite, $\text{Ca}_{0.2}\text{CrS}_2 \cdot 2\text{H}_2\text{O}$ [13] or so-called phases of A and B type $\approx (\text{Na,K})_{0.07-0.12}\text{CrS}_2 \cdot n\text{H}_2\text{O}$ [14].

Layered dichalcogenides of the transition metals often display interesting electrochemical and magnetic properties and are widely applied in both commercial contexts and basic research in the areas of battery chemistry, catalytic chemistry, solid state chemistry, thermoelectric technology, optoelectronic technology, and so on [15–17].

In the present paper, we provide the results of an investigation of the layered chromium disulfides with the common formula $M\text{CrS}_2$, where $M = \text{Na, Cu, Ag}$, which have been found in terrestrial rock for the first time, and the products of their low-temperature alteration as well as associated minerals from the phosphide-bearing breccia of the Hatrurim Complex, Israel. We also discuss the conditions and mechanisms of chromium disulfide genesis in pyrometamorphic rock.

2. Materials and Methods

More than 200 samples of phosphide-bearing breccia with fragments of black, weakly altered gehlenite paralava enriched in sulphides were collected during fieldwork in 2019 and 2021 from a small outcrop in the Negev Desert, Israel [1,18]. In all, five samples, chromium disulphides, the main object of the investigation, were detected.

The morphology and chemical composition of chromium disulfides and associated minerals were investigated using Phenom XL and Quanta 250 EDS-equipped scanning electron microscopes (Institute of Earth Sciences, University of Silesia, Poland). The mineral chemical composition was measured with a Cameca SX100 electron microprobe analyzer (EMPA, Micro-Area Analysis Laboratory, Polish Geological Institute—National Research Institute, Warsaw, Poland), WDS, accelerating voltage = 15 kV, beam current = 10–20 nA. Natural and synthetic standards were used.

The Raman spectra of the minerals were recorded on a WITec alpha 300R Confocal Raman Microscope (Institute of Earth Science, University of Silesia, Poland) equipped with an air-cooled solid laser (488 nm), a CCD camera operating at -61°C , and a monochromator with a 600 mm^{-1} grating. The power of the laser at the sample position was $\sim 4\text{--}7\text{ mW}$. Integration times of 3 s with an accumulation of 20–30 scans were chosen, and the resolution was 3 cm^{-1} . The monochromator was calibrated using the Raman scattering line of a silicon plate (520.7 cm^{-1}).

The reflected spectra of the minerals were measured with the help of the reflectometer Filmetrix coupled with the optical microscope Leica 2700P using objective $\times 100$ and Si Filmetrix standard.

3. Occurrence

Monovalent-metal chromium disulphides have been found in phosphide-bearing explosive breccia, forming a small vertical zone 4–5 m wide in layered hydrogrossular-bearing rock (“low-temperature Hatrurim”) in an outcrop on the Arad-Dead Sea road, Hatrurim Basin, Negev Desert, Israel [1]. Aggregates of the Fe-P(\pm C) system minerals barringerite, Fe_2P ($P\text{-}62m$, $hP9$), schreibersite, Fe_3P , native iron and schreibersite–iron eutectic are widely distributed in the explosive breccia of the pyrometamorphic Hatrurim Complex [1]. V-bearing andreyivanovite, FeCrP , and V-Cr-bearing allabogdanite, Fe_2P ($Pnma$, $oP12$), have also been identified in this breccia [1]. The super-reduced character of the phosphide association was confirmed by the discovery of osbornite [18], which is extremely unusual for rocks of the Hatrurim Complex, which formed under the oxidizing conditions of the sanidinite facies ($700\text{--}1400^\circ\text{C}$ and low pressure) and so are mainly composed of minerals containing trivalent iron [19].

Rocks of the pyrometamorphic Hatrurim Complex (Mottled Zone), including larnite, spurrite, and gehlenite rocks and different types of paralavas, are distributed along the Dead Sea rift in the territories of Israel, Palestine, and Jordan [20–23]. The “Classic” genetic hypothesis suggests that rocks of the Hatrurim Complex formed as a result of the burning of the bitumen substance contained in sedimentary protolith [20]. The recently proposed “Mud volcanos” hypothesis states that the activation of natural fires and the pyrometamorphic transformation of sedimentary protolith occurred with the participation of methane delivered from gas traps in the tectonically active Dead Sea rift zone [22,24].

The studied breccia consists of clasts of altered sedimentary rock transformed into porous hydrogrossular-bearing rock with relics of high-temperature minerals (pseudowollastonite, iron phosphides, and osbornite) cemented by gehlenite paralava [1,18]. As a rule, gehlenite in paralava is intensively replaced by hydrogrossular, which blurs the boundaries between clasts and breccia cement, where minerals of the Fe-P(\pm C) system concentrate (Figure 1a,b). The rounded aggregates of minerals of the Fe-P(\pm C) system exhibit a characteristic zonation from the centrum to the rim (barringerite—schreibersite—schreibersite—iron eutectic) [1] or schreibersite—iron (\pm cohenite) eutectic with relatively large iron segregations featuring rare schreibersite inclusions (Figure 1c). In the schreibersite—iron (+cohenite) eutectic, small drops of native copper (Figure 1d) and daubréelite inclusions (Figure 1e) can be observed. Aggregates of the Fe-P(\pm C) system minerals intergrow with pyrrhotite with the lamellar exsolution structure of daubréelite (Figure 1f).

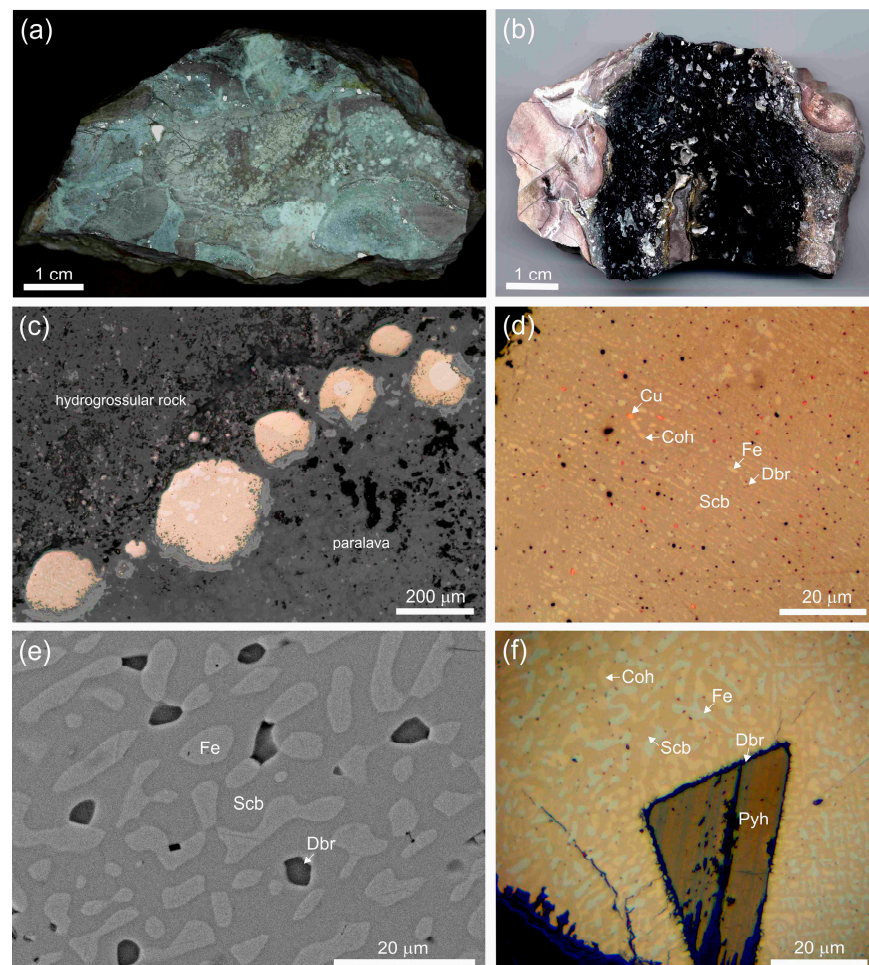


Figure 1. (a) Polished fragment of breccia, on the boundary of altered country rock clasts (brown hue) and hydrated gehlenite paralava (grey) there is a large amount of mineral aggregate of the Fe-P(\pm C) system (white). (b) Polished breccia fragment with black weakly altered gehlenite paralava.

(c) Aggregates of Fe-P(\pm C) system minerals on the boundary of paralava and altered country rock (schreibersite and barringerite, cream; native iron (\pm cohenite), white; pyrrhotite replaced for iron hydroxides, light-grey); reflected light. (d) Schreibersite (cream); native iron (white) (\pm cohenite, white with yellow hue) eutectic with native copper inclusions, rare very small daubréelite inclusions are light-grey; dark points, empties; reflected light. (e) Schreibersite–iron eutectic with daubréelite inclusions; BSE. (f) Schreibersite–iron (+cohenite) eutectic with pyrrhotite inclusion containing daubréelite lamellas; optical image with high contrast. Coh = cohenite; Cu = native copper; Dbr = daubréelite; Fe = native iron; Pyh = pyrrhotite; Scb = schreibersite.

Weakly altered paralava is black (Figure 1b). In massive fragments, native iron inclusions are predominant (Figure 2a), whereas, in porous fragments, sulphides prevail (Figure 2b). Altered sulphide aggregates contain calwellsilverite crystals (Figure 2c,d). Paralava with native iron is least altered and is represented by flamite (α' -Ca₂SiO₄)–gehlenite rock, in which only a small proportion of flamite is replaced by rankinite, Ca₃Si₂O₇ (Figure 2a). Porous paralava is predominantly composed of rankinite–gehlenite and features rare flamite relics and prismatic pseudowollastonite crystals (Figure 2b). The main accessory minerals in gehlenite paralava are Cr-Si-bearing perovskite, with the mean empirical formula being (Ca_{0.97}Na_{0.02}Sr_{0.01}) Σ 1.00(Ti⁴⁺_{0.78}Si_{0.11}Cr³⁺_{0.04}V³⁺_{0.03}Al_{0.03}Mg_{0.01}) Σ 1.00O_{2.93}, chromite with the formula (Fe²⁺_{0.78}Mg_{0.22}Ca_{0.03}Mn²⁺_{0.01}Zn_{0.01}) Σ 1.05 (Cr³⁺_{1.59}Al_{0.16}V³⁺_{0.10}Ti⁴⁺_{0.08}Si_{0.01}) Σ 1.94O₄, Cr-V-bearing pyrrhotite and fluorapatite.

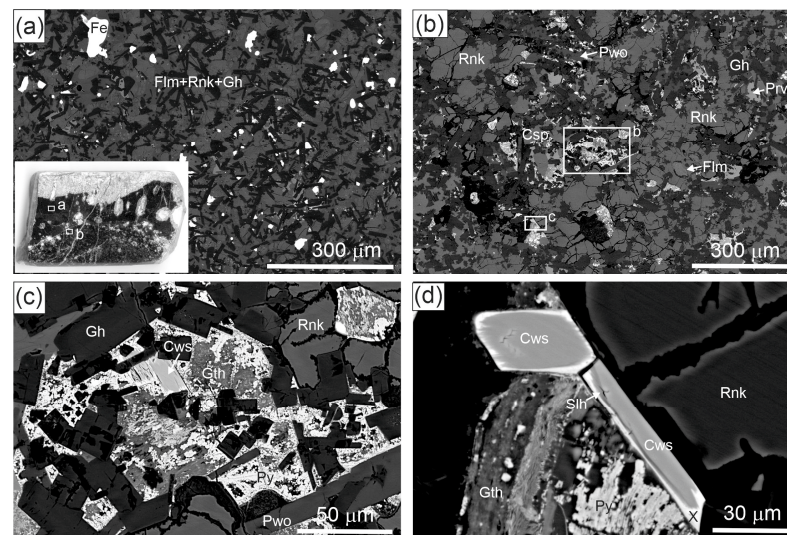


Figure 2. (a) Weakly altered massive gehlenite–flamite rock with native iron inclusions; BSE. In the inset, polished sample of gehlenite paralava, where fragments magnified in Figure 2a,b are shown. (b) Fragment of porous gehlenite–rankinite paralava enriched in sulphides with single prismatic pseudowollastonite crystals, cuspidine and flamite relics; BSE. (c) Pyrite and goethite aggregates with caswellsilverite crystals; BSE image. (d) Caswellsilverite crystals replaced by schöllhornite and “mineral X”. Csp = cuspidine; Cws = caswellsilverite; Gh = gehlenite; Gth = goethite; Fe = native iron; Flm = flamite; Prv = perovskite; Pwo = pseudowollastonite; Py = pyrite; Rnk = rankinite; Slh = schöllhornite; X = “mineral X”.

4. Chromium Disulphides

Caswellsilverite forms prismatic crystals, which are usually partially or completely replaced by “mineral X” (Figure 3a,b). Caswellsilverite crystals are grey and exhibit pronounced bireflectance (Figure 3c,d). Their reflectance varies from 21.8% to 31.0% (Figure 4, Table 1). The chemical composition of caswellsilverite (Figure 3b; Table 2) is characterised by a Na deficit compared with the ideal formula, and the mineral probably contains a small amount of water. Its empirical formula is (Na_{0.77}Sr_{0.03}Ca_{0.01}) Σ 0.81 (Cr³⁺_{0.79}Cr⁴⁺_{0.18}V³⁺_{0.01}Fe³⁺_{0.01}) Σ 0.99S₂·0.1H₂O (end-member content NaCrS₂ = 76%). The

calculated formula of “mineral X”, which forms a thin rim on caswellsilverite (Figure 3b), has a ratio of Cr/S \approx 1:2 and has an unbalanced charge (4.51+/4−). Its empirical formula is $\{(Fe^{3+}_{0.24}Si_{0.04}Al_{0.01})(Ba_{0.12}Ca_{0.10}Na_{0.05}Sr_{0.03}Zn_{0.01})\}_{\Sigma 0.60}(Cr^{3+}_{0.99}V^{3+}_{0.02})_{\Sigma 1.01}S_2 \cdot 0.74H_2O$ (Table 2). The chemical elements occupying sites between the disulphide layers $(CrS_2)^{1-}$ are those in curly brackets. Here, it should be emphasised that because of the small size of chromium disulphide grains, microprobe measurements were performed at a small beam size of 1–2 μm , which could lead to sodium and water loss in the course of an experiment. Grokhovskiyite forms exsolution lamellas in twinned pyrrhotite grains with a composition of $(Fe_{0.85}Cr_{0.02}V_{0.02}Ca_{0.01})_{\Sigma 0.90}S$ located at the wall of a gaseous channel (Figure 5). Grokhovskiyite lamellas are intensively replaced by secondary undiagnosed Cr-bearing sulphates (Figure 5), as can be clearly seen in the X-Ray maps (Figure 6, Table 3). Grokhovskiyite has unbalanced charge (4.31+/4−) and the empirical formula $\{Cu^{+}_{0.84}Fe^{3+}_{0.10}Ca_{0.06}Na_{0.01}Sr_{0.01}Ba_{0.01}\}_{\Sigma 1.03}(Cr^{3+}_{0.94}Fe^{3+}_{0.05}V^{3+}_{0.01})_{\Sigma 1.00}S_2 \cdot 0.35H_2O$ (Table 3). This is probably connected with its partial substitution by “mineral X”. Additionally, it cannot be ruled out that a pyrrhotite matrix can affect the results of the grochowskiite composition (Figure 5b). Nevertheless, 75%–80% of the content is the end-member $CuCrS_2$. “Mineral X”, replacing the grokhovskiyite plate (Figure 5b), is characterised by the empirical formula (charge 4.66+/4−): $\{(Fe^{3+}_{0.39}Al_{0.01}Si_{0.01})(Ca_{0.08}Cu^{+}_{0.05}Ba_{0.05}Sr_{0.04}K_{0.02}Na_{0.01})\}_{\Sigma 0.66}(Cr^{3+}_{0.86}Fe^{3+}_{0.13}V^{3+}_{0.01})_{\Sigma 1.00}S_2 \cdot 0.79H_2O$ (Table 3). In this cavity of paralava, there is pyrrhotite $(Fe_{0.85}Cr_{0.03}V_{0.02})_{\Sigma 0.9}S$ with intergrowths of a totally replaced chromium disulphide plate (grokhovskiyite?) (Figure 5a–c). Interestingly, in this altered sulphide aggregate, it was possible to detect caswellsilverite crystal partially replaced by “mineral X” and relics of a mineral of the djerfisherite group—Ba-bearing gmalimite, $(K,Ba)_6(Fe,Cu,Ni)_{25}S_{27}$ (Figure 5d). The chemical composition of “mineral X” from pseudomorph after grokhovskiyite has the empirical formula (charge 4.3+/4−): $\{(Fe^{3+}_{0.29}Si_{0.01})(Ba_{0.08}Ca_{0.05}Mn^{2+}_{0.02}Sr_{0.02}K_{0.01}Zn_{0.01}Cu^{2+}_{0.01}Na_{0.01})\}_{\Sigma 0.51}(Cr^{3+}_{0.95}Fe^{3+}_{0.04}V^{3+}_{0.01})_{\Sigma 1.00}S_2 \cdot 0.48H_2O$ (Table 3). Grokhovskiyite exhibits a strong bireflectance, and its reflectance varies between 27.2 and 33.0% (Table 1; Figure 6a,b). Grokhovskiyite was also detected as thin rims on caswellsilverite crystals replaced by “mineral X” (Figure 7).

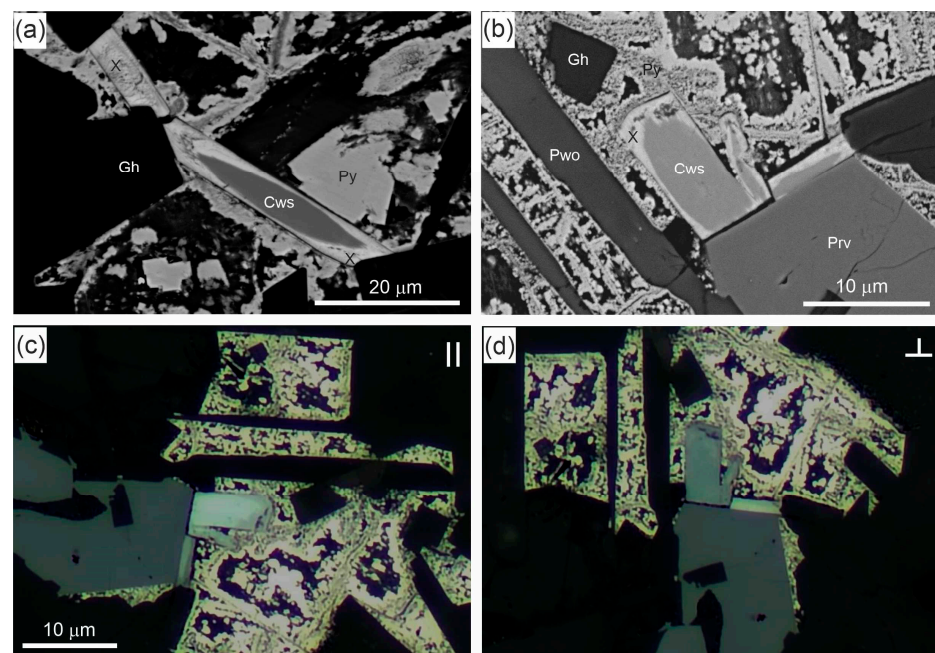


Figure 3. (a,b) Prismatic caswellsilverite crystals in sulphide aggregate; BSE. (c,d) Caswellsilverite is characterised by strong bireflectance reflected light: (c) parallel to polarizer; (d) perpendicular to polarizer. Cws = caswellsilverite; Gh = gehlenite; Prv = perovskite; Pwo = pseudowollastonite; Py = pyrite; X = “mineral X”.

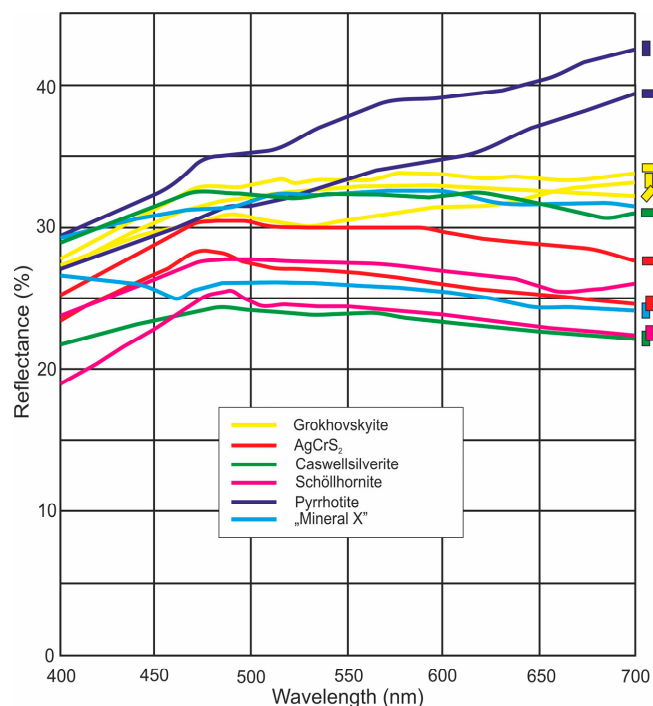


Figure 4. Reflectance spectra of chromium disulphides and pyrrhotite from gehlenite paralava. The approximate orientation of crystals during measurements is shown by rectangles on the right side of the figure.

Table 1. Reflectance of pyrrhotite (Pyh), schöllhornite (Slh), caswellsilverite (Cws), AgCrS₂ (Ag), “mineral X” (MinX) and grokhovskiyite (Ghy) measured in random sections parallel (II), perpendicular (pr) and at an angle (X) to the elongation of lamellar crystal.

nm	Pyh_II	Pyh_pr	Slh_II	Slh_pr	Cws_II	Cws_pr	Ag_II	Ag_pr	MinX_II	MinX_pr	Ghy_II	Ghy_X	Chy_pr
400	29.5	27.0	19.0	23.8	21.8	28.9	23.5	25.2	26.6	29.1	27.2	27.2	27.8
420	30.5	28.0	20.2	24.9	22.3	30.0	24.9	26.5	26.2	30.0	28.2	28.2	29.0
440	31.6	29.0	22.0	25.8	23.0	31.0	26.0	28.0	26.0	30.6	29.2	29.8	30.7
460	33.0	30.0	23.8	26.9	23.6	32.0	27.2	29.5	25.0	31.0	30.0	30.9	32.0
470 (COM)	34.0	30.3	24.8	27.3	24.0	32.4	28.0	30.2	25.5	31.1	30.2	31.1	32.8
480	35.0	31.1	25.5	27.5	24.3	32.4	28.1	30.4	25.9	31.1	30.5	31.5	32.8
500	35.1	31.4	24.8	27.6	24.0	32.1	27.4	30.4	26.0	31.6	30.5	32.0	32.9
520	35.9	31.9	24.5	27.5	23.9	32.0	27.0	30.0	26.0	32.1	30.1	32.3	33.0
540	37.1	32.9	24.4	27.5	23.9	32.3	27.0	30.0	26.0	32.1	30.1	32.6	33.1
546 (COM)	37.5	33.1	24.3	27.5	23.9	32.2	26.9	30.0	26.0	32.1	30.3	32.8	33.1
560	38.1	33.8	24.1	27.3	24.0	32.1	26.8	30.0	25.9	32.3	30.7	32.9	33.1
580	39.0	34.2	24.0	27.1	23.5	32.0	26.3	30.0	25.7	32.5	31.0	33.0	33.8
589 (COM)	39.0	34.6	23.9	27.0	23.4	32.0	26.1	30.0	25.5	32.6	31.1	33.0	33.8
600	39.0	34.8	23.8	26.9	23.2	32.0	26.0	29.8	25.3	32.6	31.3	32.9	33.7
620	39.4	35.3	23.5	26.6	23.0	32.3	25.6	29.0	25.0	32.0	31.3	32.8	33.3
640	40.0	36.7	23.0	26.1	22.8	31.9	25.3	28.9	24.6	31.5	32.0	32.7	33.4
650 (COM)	40.3	37.0	22.9	25.8	22.7	31.6	25.1	28.9	24.2	31.5	32.1	32.5	33.3
660	40.8	37.6	22.8	25.3	22.4	31.2	25.0	28.8	24.2	31.5	32.4	32.3	33.1
680	41.8	38.3	22.5	25.7	22.2	30.8	24.9	28.3	24.1	31.7	32.9	32.2	33.3
700	42.2	39.2	22.2	26.0	22.0	31.0	24.7	27.9	24.0	31.4	33.0	32.0	33.8

Table 2. Chemical composition of caswellsilverite (1) and “mineral X” (2), Figure 3b.

	1			2		1		2	
	n = 9	s.d.	range	n = 1		apfu		apfu	
Si	n.d.			0.64	S	2.00		2.00	
S	46.37	0.24	45.81–46.69	37.58	Si			0.04	
Ca	0.31	0.08	0.24–0.46	2.34	Ca	0.01		0.10	
Zn	n.d.			0.29	Zn			0.01	
Fe	0.37	0.06	0.28–0.50	7.94	Fe ³⁺	0.01		0.24	
Cr	36.65	0.36	35.89–37.13	30.18	Cr ³⁺	0.79		0.99	
V	0.33	0.02	0.30–0.35	0.49	Cr ⁴⁺	0.18			
Ti	0.13	0.07	0.08–0.30	n.d.	V ³⁺	0.01		0.02	
Al	n.d.			0.14	Al			0.01	
Na	12.70	0.52	11.82–13.75	0.60	Na	0.77		0.05	
Sr	1.82	0.03	1.78–1.88	1.66	Sr	0.03		0.03	
Ba	n.d.			9.83	Ba			0.12	
H ₂ O	1.32		0–0.23	7.80					
Total	100.00			100.00	H ₂ O	0.10		0.74	

n.d.: not detected

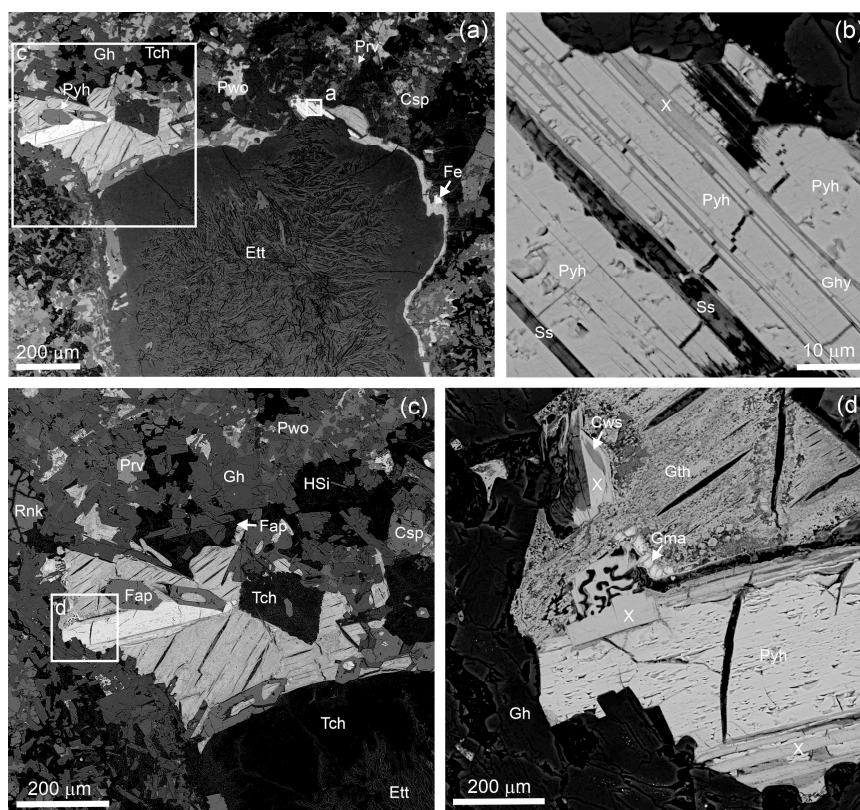


Figure 5. (a) The wall of the gaseous channel in gehlenite paralava is covered by sulphides (replaced by goethite) with native iron inclusions; the fragments shown in the frames are magnified in Figure 5b,c. (b) Lamellar pyrrhotite with parallel intergrowths of grokховskyite. (c) Pseudomorph after pyrrhotite filled with iron hydroxides and sulphates with pyrite impurity; the fragment in the frame is magnified in Figure 5d. (d) Pseudomorph after grokховskyite (?) (“mineral X”) and gmalimite relics on the boundary of goethite, pyrite and unidentified iron sulphate aggregate. BSE images. Cws = caswellsilverite; Csp = cuspidine; Ett = ettringite; Fap = fluorapatite; Gh = gehlenite; Gma = gmalimite; Gth = goethite; Ghy = grokховskyite; Fe = native iron; HSi = hydrosilicates; Prv = perovskite; Pwo = pseudowollastonite; Py = pyrite; Pyh = pyrrhotite; Rnk = rankinite; Ss = unidentified chromium sulphates; Tch = tacharanite; X = “mineral X”.

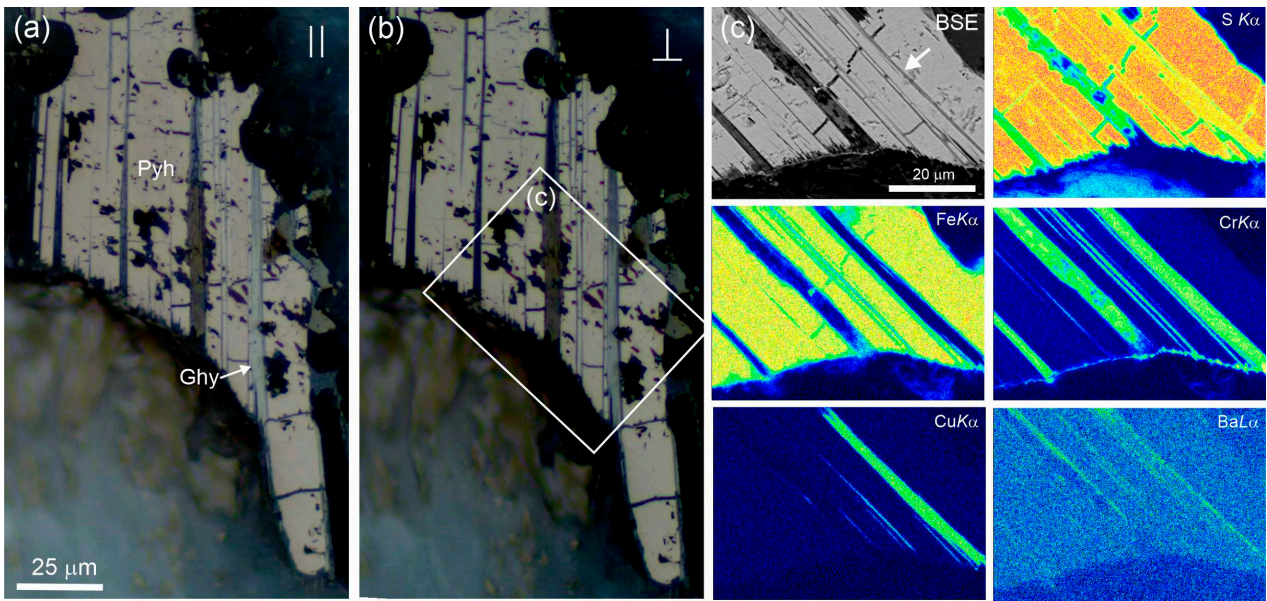


Figure 6. (a,b) Grokhovskiyte exhibits high birefractance (a—|| to polarizer, b—⊥ to polarizer), fragment magnified in Figure 6c is outlined by frame; reflected light. (c) BSE image (grokhovskiyte is shown by an arrow) and X-Ray maps of S, Fe, Cr, Cu, and Ba distribution. Pyh = pyrrhotite; Ghy = grokhovskiyte.

Table 3. Chemical composition of grokhovskiyte (1), “mineral X”(2,4) and pyrrhotite (3,5).

		Figure 5b						Figure 5d					
		1		2		3		4		5			
wt.%	mean 7	s.d.	range	mean 3	mean 7	s.d.	range	mean 8	s.d.	range	mean 7	s.d.	range
Si	n.d.			n.d.	n.d.			0.19	0.04	0.14–0.28	n.d.		
Al	n.d.			n.d.	n.d.			0.07	0.01	0.06–0.09	n.d.		
S	34.70	0.79	33.33–35.69	37.32	38.57	0.29	37.99–38.90	40.25	1.01	37.68–41.03	38.34	0.47	37.78–39.13
K	n.d.			0.41	n.d.			0.29	0.05	0.23–0.38	n.d.		
Ca	1.13	0.39	0.70–1.90	1.93	0.29	0.06	0.21–0.36	1.32	0.45	0.97–2.42	n.d.		
Zn	n.d.			0.12	n.d.			0.59	0.43	0.12–1.47	n.d.		
Cu	28.91	0.95	27.49–30.02	1.97	n.d.			0.38	0.33	0.04–0.94	n.d.		
Fe	4.41	2.38	2.52–9.96	17.03	57.35	0.31	56.67–57.56	11.62	1.06	9.99–12.96	57.38	0.58	56.34–58.10
Mn	n.d.			0.15	0.14	0.09	0.05–0.32	0.78	0.30	0.40–1.21	0.33	0.11	0.18–0.48
Cr	26.51	0.53	25.61–27.09	25.97	1.51	0.25	1.23–2.02	30.88	0.71	29.15–31.75	2.15	0.25	1.74–2.42
V	0.20	0.01	0.18–0.23	0.33	1.00	0.17	0.80–1.30	0.22	0.05	0.15–0.32	1.07	0.11	0.98–1.29
Na	0.07	0.02	0.04–0.09	0.11	n.d.			0.17	0.06	0.10–0.29	n.d.		
Sr	0.27	0.05	0.21–0.38	2.03	n.d.			1.24	0.14	1.06–1.54	n.d.		
Ba	0.45	0.12	0.20–0.62	4.07	n.d.			6.53	0.68	5.79–7.70	n.d.		
H ₂ O	3.36			8.23	n.d.			5.45			n.d.		
Total	100.00			100.00	98.87			100.00			99.28		
apfu													
Si				0.01				0.01					
Al				0.01									
S	2.00			2.00	1.00			2.00			1.00		
K				0.02				0.01					
Ca	0.05			0.08	0.01			0.05					
Zn								0.01					
Cu	0.84			0.05				0.01					
Fe	0.15			0.52	0.85			0.33			0.86		
Mn								0.02					
Cr	0.94			0.86	0.02			0.95					
V	0.01			0.01	0.02			0.01			0.02		
Na	0.01			0.01				0.01					
Sr	0.01			0.04				0.02					
Ba	0.01			0.05				0.08					
H ₂ O	0.35			0.79				0.48					

n.d.—not detected.

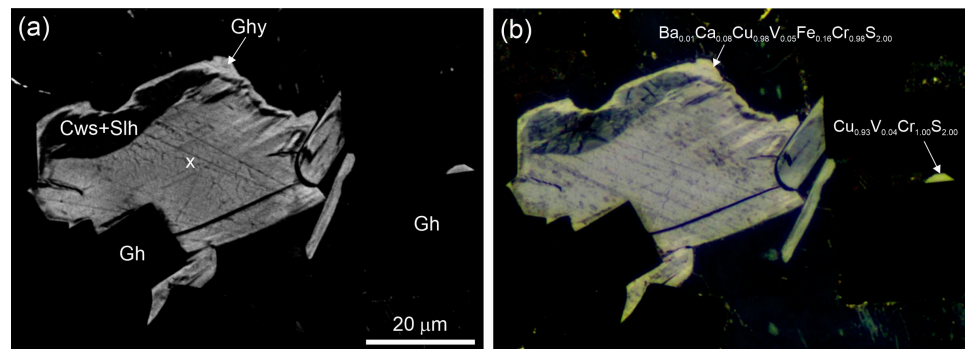


Figure 7. Grokhovskiyite forms a rim on an altered caswellsilverite crystal ((a), BSE; (b), reflected light). Cws = caswellsilverite; Gh = gehlenite; Ghy = grokhovskiyite; Slh = schöllhornite; X = “mineral X”.

A potentially new mineral Ag analogue of grokhovskiyite was found only once in gehlenite paralava, where pseudowollastonite was widely distributed (Figure 8a–c). In this paralava, especially on the boundary with the altered country rock, rounded aggregates of schreibersite–iron eutectic are intergrown with pyrrhotite containing very thin lamellas of daubréelite. In Figure 8d, the darker part of the aggregate has the composition $\sim(\text{Fe}_{0.57}\text{Cr}_{0.24}\text{V}_{0.06})_{\Sigma 0.84}\text{S}$, and the lighter part $\sim(\text{Fe}_{0.64}\text{Cr}_{0.20}\text{V}_{0.07})_{\Sigma 0.91}\text{S}$. The composition of the Ag analogue of grokhovskiyite was obtained using SEM/EDS: $(\text{Ag}^{+}_{0.89}\text{Cu}^{+}_{0.07})_{\Sigma 0.96}(\text{Cr}^{3+}_{0.98}\text{Fe}^{3+}_{0.03}\text{V}^{3+}_{0.01}\text{Ni}_{0.01})_{\Sigma 1.04}\text{S}_2$ (Table 4). The measured reflectance varies within the range of 23.5%–30.4% (Figure 4; Table 1), but the reflectance values were probably lowered as the mineral is quickly altered in air.

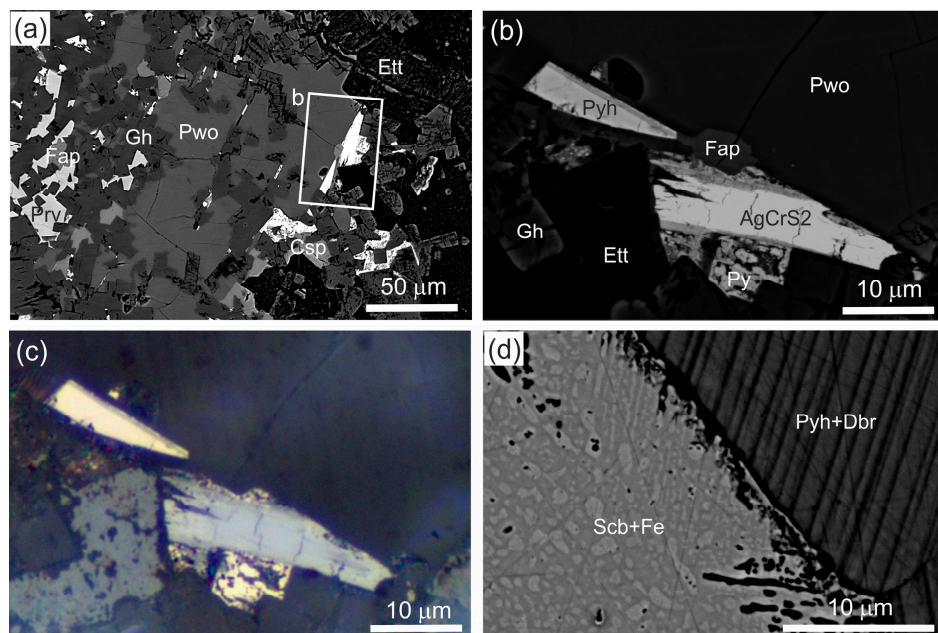


Figure 8. (a) Potentially new mineral AgCrS_2 in gehlenite–pseudowollastonite paralava. The fragment magnified in Figure 8b is outlined by the frame. (b,c) Crystal of AgCrS_2 : (b), BSE; (c), reflected light. (d) Schreibersite–iron eutectic and pyrrhotite with daubréelite lamellas from an association with AgCrS_2 . (a, b, d)—BSE; (c), reflected light. Csp = cuspidine; Dbr = daubréelite; Ett = ettringite; Fap = fluorapatite; Fe = native iron; Gh = gehlenite; Prv = perovskite; Pwo = pseudowollastonite; Pyh = pyrrhotite; Scb = schreibersite.

Table 4. Chemical composition of Ag analogue of grokhovskiyte.

wt.%	n = 14	s.d.	Range	apfu
S	29.10	1.65	25.27–31.82	2.00
V	0.25	0.15	0–0.50	0.01
Cr	23.07	1.26	20.89–24.59	0.98
Fe	0.72	0.83	0–3.10	0.03
Ni	0.31	0.35	0–1.00	0.01
Cu	2.06	0.99	0–3.60	0.07
Ag	43.60	2.91	39.91–49.85	0.89
Total	99.11			

Schöllhornite usually forms thin transition zones between caswellsilverite and “mineral X” (Figure 3d). More rarely, relatively large relics are preserved in the central part of “mineral X” pseudomorphs (Figure 9). Because of the small size of schöllhornite, microprobe measurements were performed using an electron beam size of 1–2 μm , so during the measurements, some water and sodium were lost. Analytical data were obtained for three grains (Table 5) as follows: $\{\text{Na}_{0.09}\text{Sr}_{0.03}\text{Ca}_{0.01}\}(\text{Cr}^{3+}_{0.98}\text{Fe}^{3+}_{0.01}\text{V}^{3+}_{0.01})\text{S}_2 \cdot 0.55\text{H}_2\text{O}$ (charge 3.17+/4–; Figure 9a); $\{\text{Na}_{0.16}\text{Sr}_{0.03}\text{Ca}_{0.03}\text{K}_{0.02}\text{Ba}_{0.01}\text{Sr}_{0.01}\}(\text{Cr}^{3+}_{0.96}\text{Fe}^{3+}_{0.01}\text{V}^{3+}_{0.02})\text{S}_2 \cdot 0.22\text{H}_2\text{O}$ (charge 3.31+/4–; Figure 9b); and $\{\text{Na}_{0.27}\text{Sr}_{0.03}\text{Ca}_{0.03}\text{Mn}^{2+}_{0.01}\}(\text{Cr}^{3+}_{0.98}\text{Fe}^{3+}_{0.02}\text{V}^{3+}_{0.02})\text{S}_2 \cdot 0.30\text{H}_2\text{O}$ (charge 3.47+/4–; Figure 9c).

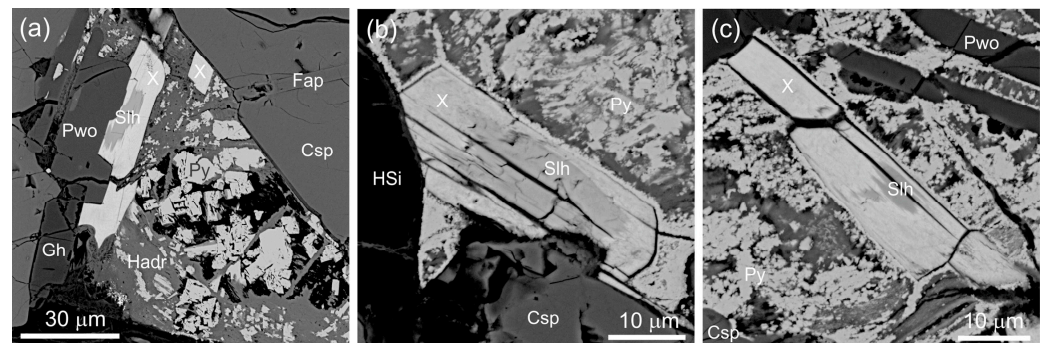


Figure 9. (a–c) Schöllhornite relics in “mineral X”; BSE. Csp = cuspidine; Fap = fluorapatite; Gh = gehlenite; Hadr = “hydroandradite”; HSi = undiagnosed hydrosilicates; Pwo = pseudowollastonite; Py = pyrite; Slh = schöllhornite; X = “mineral X”.

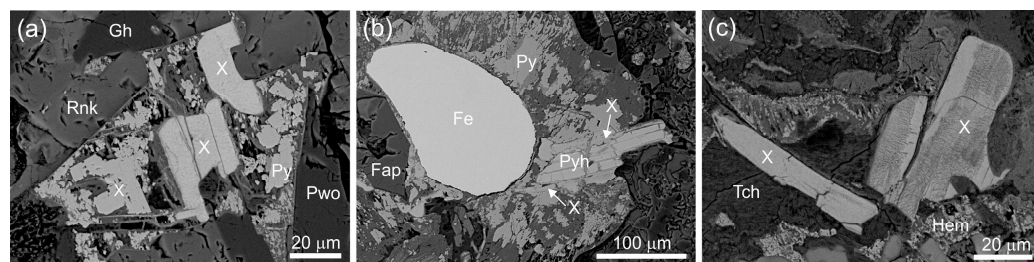
“Mineral X” replacing schöllhornite has a relatively stable composition (Table 5): $\{(\text{Fe}^{3+}_{0.31}\text{Si}_{0.02}\text{Al}_{0.01})(\text{Ba}_{0.14}\text{Ca}_{0.08}\text{Sr}_{0.03}\text{Mn}^{2+}_{0.03}\text{K}_{0.01})\}_{\Sigma 0.63}(\text{Cr}^{3+}_{0.99}\text{V}^{3+}_{0.01})\text{S}_2 \cdot 0.5\text{H}_2\text{O}$ (charge 4.61+/4–; Figure 9a); $\{(\text{Fe}^{3+}_{0.23}\text{Si}_{0.01})(\text{Ba}_{0.13}\text{Ca}_{0.04}\text{Sr}_{0.03}\text{Na}_{0.03}\text{Mn}^{2+}_{0.03}\text{K}_{0.01})\}_{\Sigma 0.63}(\text{Cr}^{3+}_{0.95}\text{V}^{3+}_{0.04}\text{Fe}^{3+}_{0.01})\text{S}_2 \cdot 0.29\text{H}_2\text{O}$ (charge 4.23+/4–; Figure 9b); and $\{(\text{Fe}^{3+}_{0.32}\text{Si}_{0.02})(\text{Ba}_{0.14}\text{Ca}_{0.06}\text{Sr}_{0.03}\text{Mn}^{2+}_{0.01}\text{K}_{0.01}\text{Na}_{0.01})\}_{\Sigma 0.63}(\text{Cr}^{3+}_{0.98}\text{V}^{3+}_{0.02})\text{S}_2 \cdot 0.41\text{H}_2\text{O}$ (charge 4.54+/4–; Figure 9c).

The composition of “mineral X” in association with pyrite ($\text{Fe}_{0.99}\text{Ni}_{0.01}\text{S}_2$) and native iron, respectively (Table 6), is as follows: $\{(\text{Fe}^{3+}_{0.33}\text{Si}_{0.02})(\text{Ba}_{0.11}\text{Ca}_{0.07}\text{Sr}_{0.03}\text{Mn}^{2+}_{0.02}\text{K}_{0.02})\}_{\Sigma 0.60}(\text{Cr}^{3+}_{0.97}\text{V}^{3+}_{0.02}\text{Fe}^{3+}_{0.01})\text{S}_2 \cdot 0.33\text{H}_2\text{O}$ (charge 4.55+/4–; Figure 10a); and $\{(\text{Fe}^{3+}_{0.38}\text{Si}_{0.01})(\text{Ba}_{0.08}\text{Ca}_{0.06}\text{Sr}_{0.05}\text{Na}_{0.02}\text{Mn}^{2+}_{0.01}\text{K}_{0.01})\}_{\Sigma 0.60}(\text{Cr}^{3+}_{0.99}\text{V}^{3+}_{0.01})\text{S}_2 \cdot 0.40\text{H}_2\text{O}$ (charge 4.61+/4–; Figure 10b).

Table 5. Chemical composition of schöllhornite (1,3,5) and “mineral X”(2,4,6) from gehlenite paralava.

wt.%	Figure 9a				Figure 9b				Figure 9c			
	1	2	s.d.	range	3	s.d.	range	4	5	6	s.d.	range
	n = 2	n = 6			n = 5			n = 3	n = 1	n = 6		
Si	0.07	0.28	0.07	0.18–0.37	0.13	0.06	0.06–0.22	0.13	0.42	0.25	0.08	0.09–0.32
Al	n.d.	0.10	0.03	0.07–0.13	n.d.			n.d.	n.d.	0.06	0.01	0.05–0.08
S	48.95	37.62	0.65	36.69–38.69	49.61	1.61	47.34–51.33	40.24	46.99	38.32	0.49	37.54–39.04
K	n.d.	0.15	0.14	0.03–0.44	0.73	0.21	0.39–0.96	0.25	0.14	0.20	0.20	0.04–0.63
Ca	0.36	1.80	0.30	1.37–2.24	0.96	0.68	0.38–2.30	1.07	0.80	1.48	0.28	0.92–1.81
Fe	0.24	10.27	0.70	8.84–11.06	0.30	0.04	0.24–0.33	8.40	0.74	10.82	0.44	10.11–11.46
Mn	n.d.	1.00	0.44	0.59–1.93	n.d.			1.07	0.48	0.42	0.14	0.26–0.66
Cr	39.05	30.16	0.54	29.28–30.99	38.78	1.03	37.20–39.76	31.02	37.45	30.32	0.30	29.87–30.75
V	0.31	0.35	0.09	0.26–0.50	0.79	0.15	0.59–0.97	1.16	0.62	0.65	0.19	0.42–1.01
Na	1.57	0.06	0.01	0.05–0.08	2.92	1.98	1.25–6.75	0.42	4.61	0.08	0.05	0.04–0.19
Sr	1.88	1.68	0.02	1.64–1.71	2.13	0.41	1.86–2.93	1.78	2.03	1.69	0.04	1.64–1.77
Ba	n.d.	11.22	0.63	10.34–12.05	0.58	0.84	0.03–2.24	11.21	1.35	11.35	0.96	9.44–12.54
H ₂ O	7.58	5.32			3.08			3.25	4.38	4.36		
Total	100.00	100.00			100.00			100.00	100.00	100.00		
Si		0.02			0.01			0.01	0.02	0.02		
apfu												
Al		0.01										
S	2.00	2.00			2.00			2.00	2.00	2.00		
K		0.01			0.02			0.01		0.01		
Ca	0.01	0.08			0.03			0.04	0.03	0.06		
Fe	0.01	0.31			0.01			0.24	0.02	0.32		
Mn		0.03						0.03	0.01	0.01		
Cr	0.98	0.99			0.96			0.95	0.98	0.98		
V	0.01	0.01			0.02			0.04	0.02	0.02		
Na	0.09				0.16			0.03	0.27	0.01		
Sr	0.03	0.03			0.03			0.03	0.03	0.03		
Ba		0.14			0.01			0.13	0.01	0.14		
H ₂ O	0.55	0.50			0.22			0.29	0.33	0.41		

n.d.—not detected.

**Figure 10.** (a–c) Character of “mineral X” morphology; BSE images. Fe = native iron; Gh = gehlenite; Pyh = pyrrhotite; Py = pyrite; Fap = fluorapatite; Hem = hematite; Tch = tacharanite; Rnk = rankinite; Pwo = pseudowollastonite; X = “mineral X”.

“Mineral X” is a potentially new mineral, which replaces caswellsilverite and grokhovskyite, often forming full pseudomorphs (Figure 10c). The composition of its main components varies considerably but has a constant ratio of $\text{Cr}(\pm\text{V}, \text{Fe})/\text{S} = 1:2$: $\{\text{Fe}_{0.23-0.38}\text{Ba}_{0.08-0.14}\text{Ca}_{0.04-0.10}\text{Sr}_{0.02-0.05}\text{Na}_{0-0.05}\text{Mn}_{0-0.03}\}(\text{Cr}_{0.95-0.99}\text{V}_{0.01-0.04}\text{Fe}_{0-0.04})\text{S}_2 \cdot (\text{H}_2\text{O})_{0.29-0.74}$, with traces of Al, Si, Cu, Zn, K (Tables 5 and 6). The mean crystal–chemical formula is $\{\text{Fe}^{3+}_{0.31}\text{Ba}_{0.11}\text{Ca}_{0.07}\text{Sr}_{0.03}\text{Mn}^{2+}_{0.02}\text{Na}_{0.02}\}(\text{Cr}^{3+}_{0.97}\text{V}^{3+}_{0.02}\text{Fe}^{3+}_{0.01})\text{S}_2 \cdot 0.45\text{H}_2\text{O}$.

We failed to extract crystals of the studied minerals for a structural investigation; therefore, to obtain information about their structural features, we used Raman spectroscopy.

Table 6. Chemical composition of “mineral X” (1,4), pyrite (2,6), native iron (3), and pyrrhotite (5).

	Figure 10a			Figure 10b					Figure 10c					
	1			2	3	4		5		6				
wt.%	mean 5	s.d.	range	mean 2	mean 4	mean 8	s.d.	range	mean 5	s.d.	range	mean 5	s.d.	range
Si	0.29	0.10	0.17–0.42	n.d.	n.d.	0.18	0.07	0.08–0.30	n.d.			n.d.		
Al	0.06	0.01	0.05–0.07	n.d.	n.d.	n.d.	n.d.		n.d.			n.d.		
S	38.97	0.47	38.29–39.53	53.15	n.d.	39.18	0.34	38.79–39.79	38.98	0.12	38.86–39.20	53.28	0.31	52.71–53.62
K	0.58	0.14	0.42–0.85	n.d.	n.d.	0.24	0.12	0.06–0.49	n.d.			n.d.		
Ca	1.66	0.22	1.38–1.92	0.27	n.d.	1.57	0.38	1.08–2.29	n.d.			n.d.		
Cu	n.d.			0.19	n.d.	n.d.	n.d.		n.d.			0.16	0.03	0.13–0.22
Ni	n.d.			0.33	1.63	n.d.	n.d.		n.d.			0.14	0.04	0.09–0.21
Co	n.d.			n.d.	0.27	n.d.	n.d.		n.d.			n.d.		
Fe	11.67	0.41	11.16–12.33	46.53	98.05	12.94	0.67	12.09–14.26	57.58	0.24	57.26–57.92	46.84	0.19	46.52–47.12
Mn	0.66	0.33	0.41–1.26	n.d.	n.d.	0.39	0.20	0.11–0.78	0.41	0.12	0.28–0.57	n.d.		
Cr	30.68	0.73	29.67–31.75	n.d.	0.10	31.32	0.35	30.75–31.84	1.84	0.20	1.61–2.09	0.10	0.14	0.02–0.37
V	0.77	0.29	0.32–1.12	n.d.	n.d.	0.26	0.06	0.19–0.37	1.21	0.11	1.08–1.35	n.d.		
Na	0.05	0.03	0.03–0.11	n.d.	n.d.	0.23	0.20	0.06–0.63	n.d.			n.d.		
Sr	1.65	0.04	1.62–1.71	n.d.	n.d.	2.77	0.55	2.08–3.79	n.d.			n.d.		
Ba	9.35	0.60	8.51–10.05	n.d.	n.d.	6.51	1.82	3.40–8.90	n.d.			n.d.		
H ₂ O	3.61					4.42								
Total	100.00			100.46	100.05	100.00			100.02			100.52		
Si						0.01								
apfu	0.02													
S	2.00			2.00		2.00			1.00			2.00		
K	0.02					0.01								
Ca	0.07			0.01		0.06								
Ni				0.01	0.02									
Fe	0.34			1.00	0.98	0.38			0.85			1.01		
Mn	0.02					0.01			0.01					
Cr	0.97					0.99			0.03					
V	0.02					0.01			0.02					
Na						0.02								
Sr	0.03					0.05								
Ba	0.11					0.08								
H ₂ O	0.33					0.40								

n.d.—not detected.

5. Raman Investigation of Layered Chromium Disulphides

In the Raman spectra of caswellsilverite, there are two strong bands from Cr-S vibrations typical for the spectra of synthetic NaCrS₂: 316 (A₁) and 252 cm⁻¹ (E_g) [25]. An orientation effect is observed: the band at 316 cm⁻¹ polarizes, and its intensity drops by a factor of three times at polarization of the laser beam perpendicular to the direction of the flattening crystal (Figure 11a,b). To avoid artefacts in the spectra of the studied minerals, we also obtained their spectra after the laser-induced heating in air. The Raman spectrum of thermally changed caswellsilverite is related to sodium chromate. The strongest band in the spectrum at about 850 cm⁻¹ is related to A₁ vibrations in (CrO₄)²⁻ [26–29] (Figure 11c).

The Raman spectra of grokhovskiyite were measured on lamellar crystal in two orientations (Figure 12). The spectra featured weak bands at 315/319 cm⁻¹ (A₁) and 253/251 cm⁻¹ (E_g), which are typical for synthetic CuCrS₂ [30,31].

The bands in the Raman spectrum of the potentially new mineral AgCrS₂ (Figure 13) had a weak intensity that can be explained by its surface quality due to high instability in the ambient conditions (Figure 8c). There are also bands in the spectrum related to Cr-S vibration: 644, 320 (A₁), 279(?) и 250 (E_g) cm⁻¹ [25,32–34].

We measured the Raman spectra of schöllhornite and “mineral X” and their products as a result of thermal change under the laser beam (Figure 14). It should be emphasised that in no case did we observe active vibrational modes from OH/H₂O.

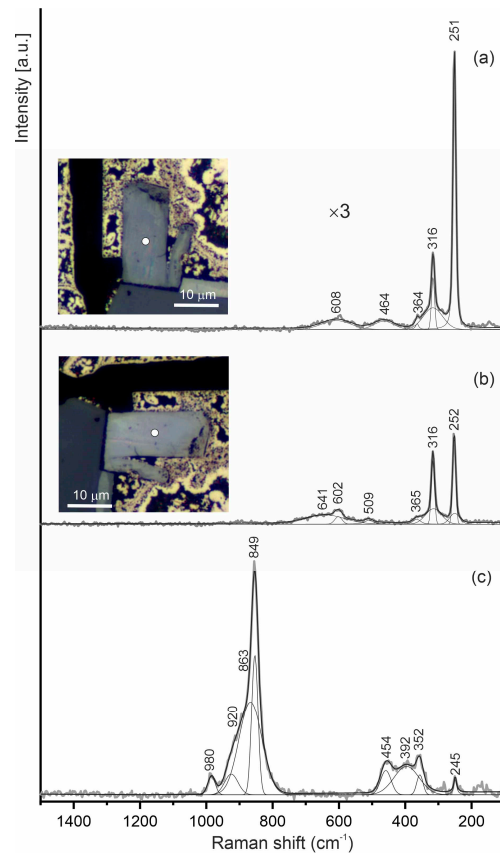


Figure 11. (a,b) Raman spectra of caswellsilverite in two orientations: perpendicular (a) and parallel (b) to the polarized incident laser beam. Spots of Raman spectra measurement are shown by white circles in reflected light images. (c) Raman spectrum obtained after thermal laser effect.

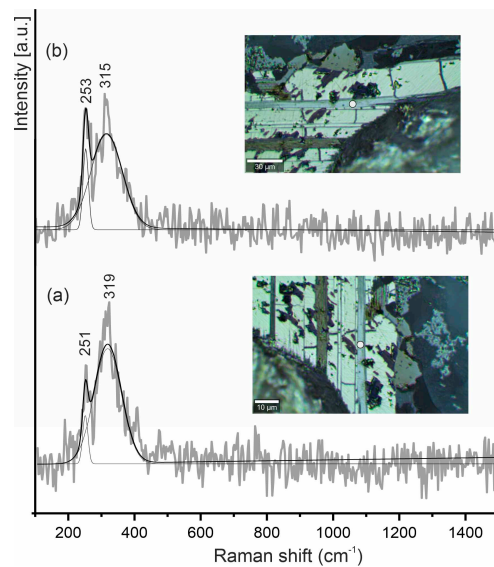


Figure 12. Raman spectra of grokhovskiyite in two orientations: perpendicular (a) and parallel (b) to the polarized incident laser beam. Points of spectra measurements are marked by white circles in reflected light images.

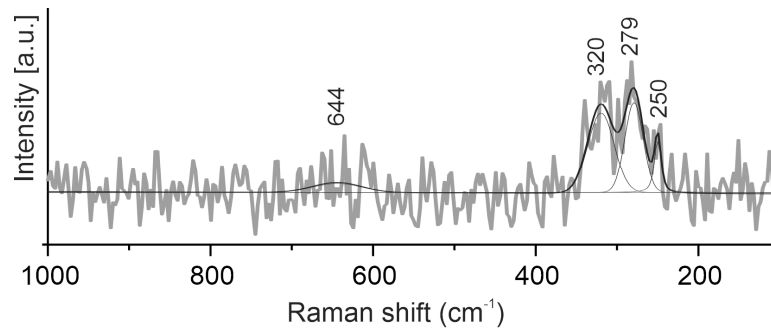


Figure 13. Raman spectrum of potentially new mineral AgCrS₂.

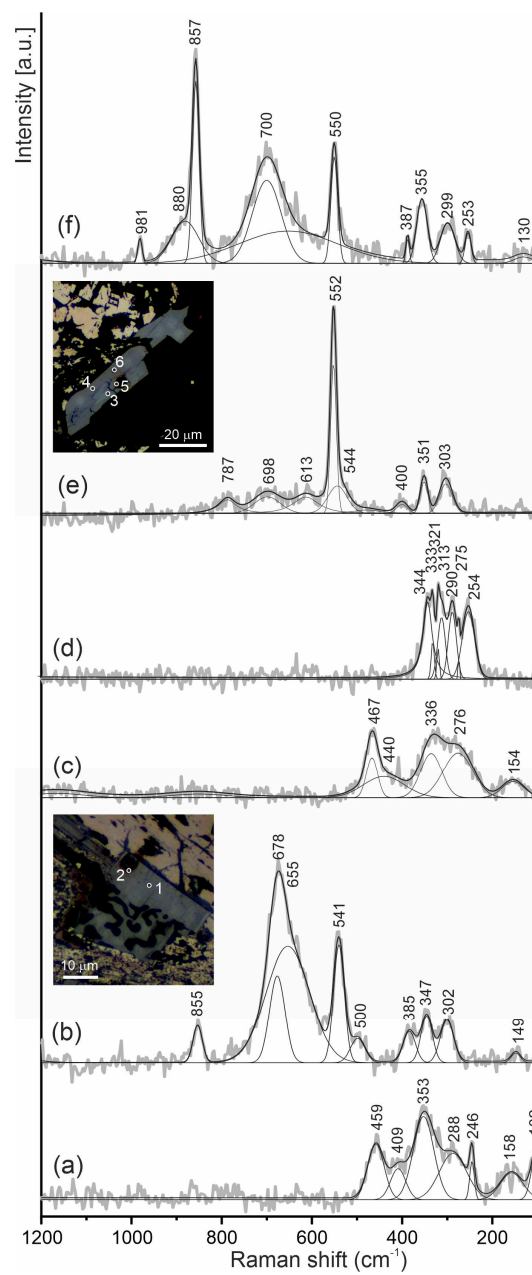


Figure 14. Raman spectra of caswellsilverite replacement products: (a,b,d,f)—“mineral X” ((a,d): original; (b,f): thermally effected); (c,e): schöllhornite ((c), original; (e), after thermal effect).

In the schöllhornite spectrum (Figure 14c), there were two strong bands at 336 and 276 cm^{-1} related to vibrations A_1 and E_g in the $(\text{CrS}_2)^-$ layers, and there was a strong band near 467 cm^{-1} , which may correspond to the S-S bond [34]. An effect of the dimerization of sulphur was noted in $\text{NaCr}_{2/3}\text{Ti}_{1/3}\text{S}_2$ disulphide as a result of the migration of Cr to the Na-vacancies [35]. It is interesting that schöllhornite, thermally affected by the Raman microscope laser beam, was replaced by esolaite, Cr_2O_3 (Figure 14e).

Non-oriented Raman spectra for “mineral X” were obtained for its full pseudomorph after disulphide, probably grokhovskiyite (Figure 14a), with the empirical formula $\{\text{Fe}^{3+}_{0.30}\text{Ba}_{0.08}\text{Ca}_{0.06}\text{Sr}_{0.02}\text{Si}_{0.02}\text{Mn}^{2+}_{0.02}\text{Cu}_{0.01}\text{Zn}_{0.01}\text{Al}_{0.01}\text{Na}_{0.01}\}(\text{Cr}_{0.95}\text{Fe}^{3+}_{0.04}\text{V}^{3+}_{0.01})\text{S}_2 \cdot 0.53\text{H}_2\text{O}$ (Table 3), and for a rim around schöllhornite (Figures 9a and 14d) with the composition $\{\text{Fe}^{3+}_{0.31}\text{Ba}_{0.14}\text{Ca}_{0.08}\text{Sr}_{0.03}\text{Mn}^{2+}_{0.03}\text{Si}_{0.02}\text{Al}_{0.01}\text{K}_{0.01}\}(\text{Cr}_{0.99}\text{V}^{3+}_{0.01})\text{S}_2 \cdot 0.50\text{H}_2\text{O}$ (Table 5). These compositions are similar and can be described by the simplified formula $\sim \{\text{Fe}_{0.3}\text{R}^{2+}_{0.2-0.3}\}\text{CrS}_2 \cdot 0.5\text{H}_2\text{O}$, $\text{R}^{2+} = \text{Ba}, \text{Sr}, \text{Ca}$. Nevertheless, their spectra differ significantly. These differences can be related both to the orientation effect and to features of the occupation of space between the $(\text{CrS}_2)^{1-}$ layers and changes in the Cr valence state. The Raman spectrum of the full pseudomorph of “mineral X” after caswellsilverite (?) resembles that of schöllhornite (Figure 14a,c). It contains the bands (cm^{-1}): 459, 409, 353, 288, 246, 158 and 102. Band 459 cm^{-1} is related to S-S vibrations [34]. On the spectrum of the phase from the rim, there is a series of bands in the range 250–350 cm^{-1} , corresponding to Cr-S vibrations in the disulphide layers (cm^{-1}): 254, 275, 290, 313, 321, 333, 344. It is notable that after laser heating, the spectra of caswellsilverite and “mineral X” visually differed (Figure 14b,f). However, in both spectra, three main vibrational modes related to the three new-formed phases can be distinguished: near 855 cm^{-1} : $(\text{CrO}_4)^{2-}$, chromate; 680–700 cm^{-1} , phase of the ACrO_3 -type; and 540–550 cm^{-1} : (Cr_2O_3) [36–38].

The Raman investigation of the natural chromium disulphides NaCrS_2 , AgCrS_2 , and CuCrS_2 confirmed their identity with the synthetic analogues (Figures 11–13).

6. Genesis and Alteration of Chromium Disulphides in Pyrometamorphic Rock

Highly reducing conditions in the terrestrial pyrometamorphic combustion process is a rare phenomenon that leads to the appearance of minerals typical for meteorites [1,18,39]. “Meteoritic” minerals, mainly phosphides, form at the contact facies of black, reduced pyrrhotite-bearing Hatrurim Complex paralavas intruded into the country rocks containing carbonaceous matter, which play the role of reductant [1,18]. It should be emphasised that yellow-green, brown oxidized paralavas with a mineral composition close to that of black paralava are widespread in the Hatrurim Complex, especially in the Hatrurim Basin, and contain mainly Fe^{3+} -bearing minerals [19].

Combustion processes during pyrometamorphism of a large area, as in the case of the Hatrurim Complex, determine the formation of a significant volume of reducing gases (CH_4 , H_2 , H_2S , CO , NO) as a result of the pyrolytic decomposition of organic matter (bitumen, oil) contained in the sedimentary protolith. The crystallization of highly reduced phases proceeds along the paths of flow of reducing gases. For example, small crystals of oldhamite, CaS , formed on the walls of micron-sized channels penetrating spurrite marble of the Hatrurim Basin [40]. Sometimes reducing gases have a significant effect on pyrometamorphic rocks, which is expressed in the crystallization of rock-forming oldhamite in larnite rock (Figure 15a) by the reaction: $\text{CaO} + \text{H}_2\text{S}_{\text{gas}} = \text{CaS} + \text{H}_2\text{O}_{\text{gas}}$. In larnite rock, oldhamite is associated with Fe^{3+} -bearing minerals such as brownmillerite, $\text{Ca}_2\text{FeAlO}_5$ (Figure 15a), and cannot be an indicator of the reduction conditions for the entire rock volume.

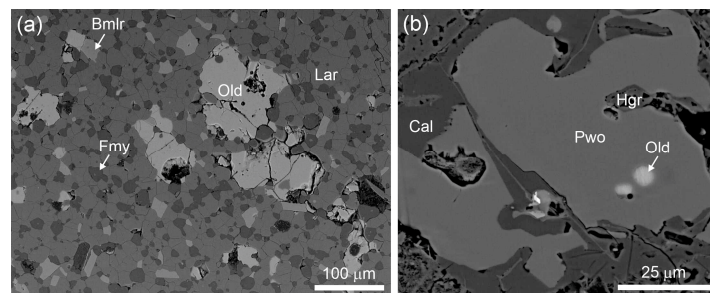


Figure 15. (a) Oldhamite-bearing fluormayenite–larnite rock from the Hatrurim Basin (Har Parsa Mt.). (b) Inclusion of oldhamite in pseudowollastonite from phosphide-bearing breccia. Bmlr = brownmillerite; Cal = calcite; Fmy = fluormayenite; Hgr = hydrogrossularite; Lar = larnite; Old = oldhamite; Pwo = pseudowollastonite.

In considering the super- and high-reduced mineral associations in pyrometamorphic rocks, two main forms of “meteorite” mineral formation should be taken into account: (1) mineral formation reactions following the short-distance transport of reacting components on the contact of hot paralava and country rock containing the reductant (carbonaceous matter); (2) mineral formation as a result of reducing gases reacting with minerals of the early “clinker” association.

The generation of gehlenite paralava with “meteoritic” chromium disulphides took place at the combustion foci at a high temperature (probably higher than 1500 °C) and low pressure [1]. An intrusion of paralava into brecciated clay-carbonate sedimentary rock containing phosphatised and graphitized organic matter as well as iron oxides caused the formation of mineral aggregates of the Fe-P(+C, Cr, V) system on the boundary of paralava and country rock (Figure 1a–c) as a result of high-temperature carbothermal reduction reactions [1,18]. On iron phosphide aggregates presented by barringerite, and schreibersite, the rim of the Fe-schreibersite eutectic was formed. This is where the monosulphide phase, which later transforms into lamellar pyrrhotite and daubréelite aggregates (Figures 1f and 8d), was detected. In rare cases, phosphides and pyrrhotite associate with osbornite, TiN—a mineral-indicator of the super-reducing conditions ($fO_2 < \text{iron-wüstite buffer } \Delta IW \approx -6$) [18,41].

In the studied phosphide-bearing breccia, a “meteoritic” sulphide, oldhamite, CaS, rarely encountered as small rounded inclusions in pseudowollastonite from the paralava contact zone, crystallizes from melt (Figure 15b), and can be an indicator of the reducing conditions. The investigation of sulphide genesis in “mercurian melt” showed that oldhamite is stable at about $\Delta IW \approx -2$ [42].

Caswellsilverite crystallizes in the central porous parts of paralava together with pyrrhotite (Figure 2b), whereas in non-porous fragments of paralava, small iron drops form (Figure 2a) that can indicate that the primary iron melt is enriched in sulphur carried by combustion gases. Experimental studies indicate that caswellsilverite (and grokhovskiyite) form in paralava at relatively higher oxygen activity $0 \leq \Delta IW < -2$ in comparison with oldhamite [42]. This suggests that super- or high-reduction conditions ($\Delta IW \approx -6$ – -2) at the contact zone of paralava with clasts of altered country rock change within a distance of a few centimetres (the central parts of paralava zones) to the reduction conditions near the Fe/FeO ($\Delta IW \approx 0$) buffer. Caswellsilverite and pyrrhotite crystallize from sulphide melt mosaically distributed in paralava between previously crystallized silicates (Figure 2b,c). Sodium, which is necessary for caswellsilverite genesis, is probably introduced into the same portion of the sulphide melt as a result of the replacement of flamite, $Ca_{2-x}(Na,K)_x(Si_{1-x}P_x)O_4$ by rankinite, $Ca_3Si_2O_7$ [18]. In experiments, $NaCrS_2$ crystals were obtained from alkaline polysulfide melt at temperatures below 1000 °C. It was also shown that they decompose slowly in the atmosphere at room temperature and are relatively quickly oxidized at temperatures above 1000 °C with the formation of $NaCrO_2$ and

Cr_2O_3 crystals [43]. Both types of caswellsilverite high-temperature alteration products were observed to form due to the thermal effect of the Raman probe (Figures 11 and 14).

In a previous analysis of the conditions of the genesis of Cr-V-bearing phosphides (barringerite, allabogdanite, andreyivanovite) in the same breccia, it was suggested that high-reduction conditions are necessary for the enrichment of Fe(+P) melt by Cr and V [1]. Additionally, we noted a local enrichment of Fe(\pm P, C) melt by Cu (Figure 1d). All these observations can be applied to sulphide melts, the crystallization of which between previously formed gehlenite crystals (Figure 2b,c), on solidified Fe drops (Figure 10b) and wall cavities (Figure 5a) led to the formation of Fe-monosulfide with a higher Cr(+Cu) concentration. Later, monosulfide transformed into lamellar polysynthetic aggregates of pyrrhotite with the grokhovskiyite exsolution structures (Figure 5b). The local enrichment of sulphide melt by Ag led to the crystallization of a potentially new mineral AgCrS_2 (Figure 8).

Hexagonal octahedral layers $(\text{CrS}_2)^{1-}$, between which *M*-sites of the monovalent cations Ag, Cu, and Na set, are present in the structures of layered chromium disulphides, MCrS_2 (Figure 16), [44–48]. The sodium is at the octahedral coordination, whereas Cu and Ag are in the deformed tetrahedra. There are two types of tetrahedral site: α - and β - (Figure 16b) [45–49]. Ordered disulphide forms at temperatures below $\sim 500^\circ\text{C}$ as a result of the occupation of the first type of site. In CuCrS_2 , an effect of some Cr moving into the space between disulphide layers was observed [45] (Figure 16c).

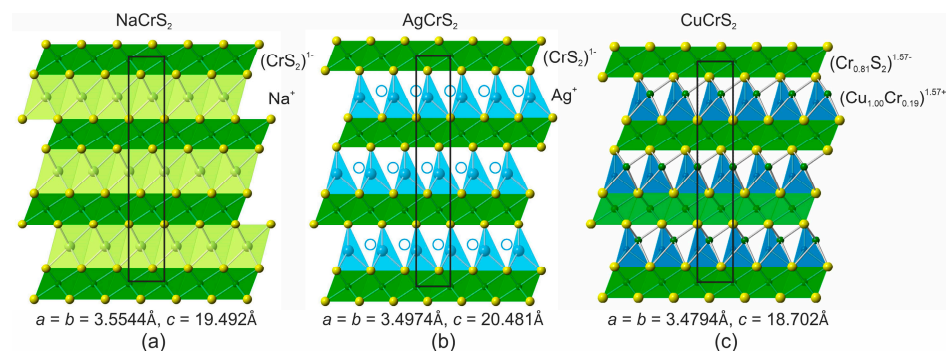


Figure 16. Structures of trigonal synthetic layered chromium disulphides, projection on (010): (a) Caswellsilverite analogue [44]; (b) analogue of potentially new mineral AgCrS_2 [44], chromium occupies tetrahedral sites of the β -type, empty circles show vacancy sites of the α -type; (c) analogue of grokhovskiyite with vacancies in Cr-disulphide layer, fully occupied Cu-tetrahedral sites and additional Cr-sites (deformed octahedron, green balls) in cation layer [45]. Atoms/polyhedra are shown in green for Cr; dark blue for Cu; light blue for Ag; light yellow for Na; and yellow for S.

Low-temperature alterations of layered chromium disulphides are exclusively reflected in changes to the composition and structure of the monovalent cation layer, whereas the hexagonal octahedral layer $(\text{CrS}_2)^{1-}$ stays practically unaltered (Tables 2, 3, 5 and 6). Hydrated products of synthetic NaCrS_2 were experimentally studied [49], and later they were discovered in meteorites as the natural minerals schöllhornite, $\text{Na}_{0.3}\text{CrS}_2 \cdot \text{H}_2\text{O}$ [12], phases of A and B type $\approx (\text{Na,K})_{0.07-0.12}\text{CrS}_2 \cdot n\text{H}_2\text{O}$ [14] and cronosite, $\text{Ca}_{0.2}\text{CrS}_2 \cdot (\text{H}_2\text{O})_2$ [13]. Caswellsilverite and grokhovskiyite in gehlenite paralava are replaced by the potentially new “mineral X” with high Fe content. This process proceeds simultaneously with pyrrhotite oxidation (Fe source) and through an intermediate phase of schöllhornite-type (Tables 2 and 3; Figures 2d, 3a and 5b). “Mineral X” has a variable (non-stoichiometric) composition (Figures 2, 3, 5 and 6), but nevertheless, its composition can be described by a non-idealized formula $\{\text{Fe}_{0.3}(\text{Ba,Ca})_{0.2}\}\text{CrS}_2 \cdot 0.5\text{H}_2\text{O}$, whose charge can be balanced only if all Fe is represented by the Fe^{2+} cation or the $\text{Fe}^{3+}(\text{OH})^-$ complex. The appearance of Fe^{2+} in Fe^{3+} -hydroxide aggregates replacing pyrrhotite is hardly probable, and this mineral needs further investigation. Schöllhornite was found at the central part of pseudomorphs

of “mineral X” after caswellsilverite (Figure 9) and also as thin zones between the “mineral X” rim and the caswellsilverite core (Figure 2d). The sum of cations (Na+Sr+Ca+Ba+Fe) in the intermedium layer of caswellsilverite varied from 0.14 (Na = 0.09) to 0.35 (Na = 0.27) apfu (Table 5).

The content of water in “mineral X” and caswellsilverite was calculated on the basis of microprobe analyses as a difference of a total of 100%. The water content of “mineral X” is lower than that of caswellsilverite or cronusite. This can be connected both with the conditions of the microprobe analyses and with genuinely low water concentrations in altered layered sulphides in a hot desert climate.

In conclusion, the necessary conditions for the appearance of “meteoritic” chromium disulphides in terrestrial rock are high chromium content, high temperatures up to ~1500 °C, low pressure, and high reducing formation conditions, i.e., conditions usually realized in the processes of meteorite genesis.

Author Contributions: E.V.G. and I.O.G. discovered the layered chromium disulfides, the main idea of the article, performed the optical and Raman investigation and wrote the article. Y.V. carried out the fieldwork, geological description and verification of the data. G.Z. performed the microprobe analyses. All authors have read and agreed to the published version of the manuscript.

Funding: The investigations were supported by the National Science Center of Poland Grant [grant number 2021/41/B/ST10/00130].

Data Availability Statement: At the request of other researchers, the authors of the article can provide the original data.

Acknowledgments: The authors thank the reviewers for their constructive remarks, which improved the original manuscript.

Conflicts of Interest: The authors declare no conflict of interest.

References

- Galuskin, E.V.; Kusz, J.; Galuskina, I.O.; Książek, M.; Vapnik, Y.; Zieliński, G. Discovery of terrestrial andreyivanovite, FeCrP, and the effect of Cr and V substitution in barringerite-allabogdanite low-pressure transition. *Am. Mineral.* **2023**, *107* (in press). [\[CrossRef\]](#)
- Okada, A.; Keil, K. Caswellsilverite, NaCrS₂: A new mineral in the Norton County enstatite achondrite. *Am. Mineral.* **1982**, *67*, 132–136.
- Grossman, J.N.; Rubin, A.E.; Rambaldi, E.F.; Rajan, R.S.; Wasson, J.T. Chondrules in the Qingzhen type-3 enstatite chondrite: Possible precursor components and comparison to ordinary chondrite chondrules. *Geochim. Cosmochim. Acta* **1985**, *49*, 1781–1795. [\[CrossRef\]](#)
- Brearely, A.J.; Jones, R.H. Chondritic meteorites. In *Planetary Materials*; Papike, J.J., Ed.; Mineralogical Society of America: Washington, DC, USA, 1998; pp. 3–398. [\[CrossRef\]](#)
- Bunch, T.E.; Irving, A.J.; Wittke, J.H.; Kuehner, S.M. Zincian breznaitite and other rare minerals in two cumulate-textured aubrites from Northwest Africa. *Meteorit. Planet. Sci. Suppl.* **2008**, *43*, 5309.
- Fahey, A.; Huss, G.R.; Wasserburg, G.J.; Lodders, K. REE abundances and CR isotopic composition of oldhamite and associate minerals from the Pena Blanca Spring Aubrite. *Abstr. Lunar Planet. Sci. Conf.* **1995**, *26*, 385.
- El Goresy, A.; Yabuki, H.; Ehlers, K.; Woolum, D.; Pernicka, E. Qingzhen and Yamato-691: A tentative alphabet for the EH chondrites. *Proc. NIPR Symp. Antarct. Meteor.* **1988**, *1*, 65–101.
- Sharygin, V. Phase CuCrS₂ in iron meteorite Uakit (IIAB), Buryatia: Preliminary data. In Proceedings of the IX Russian Young Scientists Conference “Minerals: Structure, properties, investigation methods”, Ekaterinburg, Russia, 5–8 February 2018; p. 229.
- Sharygin, V.V.; Yakovlev, G.A.; Seryotkin, Y.V.; Karmanov, N.S.; Novoselov, K.A.; Karabanalov, M.S. Grokhovskiyite, IMA 2019-065. CNMNC Newsletter No. 52. *Mineral. Mag.* **2019**, *83*, 890.
- Bevan, A.W.; Downes, P.J.; Henry, D.A.; Verrall, M.; Haines, P.W. The Gove relict iron meteorite from Arnhem Land, Northern Territory, Australia. *Meteorit. Planet. Sci.* **2019**, *54*, 1710–1719. [\[CrossRef\]](#)
- Lin, Y.T.; Al Goresy, A.; Hatcheon, I.D. The first meteoritic silver mineral in Peña Blanca Springs enstatite achondrite: Assemblage, composition and silver isotopes. *Abstr. Lunar Planet. Sci. Conf.* **1989**, *20*, 572.
- Okada, A.; Keil, K.; Leonard, B.F.; Hutcheon, I.D. Schöllhornite, Na_{0.3}(H₂O)₁[CrS₂], a new mineral in the Norton County enstatite achondrite. *Am. Mineral.* **1985**, *70*, 638–643.
- Britvin, S.N.; Guo, X.Y.; Kolomensky, V.D.; Boldyreva, M.M.; Kretser, Y.L.; Yagovinka, M.A. Cronusite, Ca_{0.2}(H₂O)₂CrS₂, a new mineral from the Norton County enstatite achondrite. *Proc. Russ. Mineral. Soc.* **2001**, *130*, 29–36.
- Kimura, M.; Lin, Y.-T.; Ikeda, Y.; El Goresy, A.; Yanai, K.; Kojima, H. Mineralogy of Antarctic aubrites, Yamato-793592 and Allan Hills-78113: Comparison with non-Antarctic aubrites and E-chondrites. *Proc. NIPR Symp. Antarct. Meteor.* **1993**, *6*, 186–203.

15. Wilson, J.A.; Yoffe, A.D. The transition metal dichalcogenides discussion and interpretation of the observed optical, electrical and structural properties. *Adv. Phys.* **1969**, *18*, 193–335. [[CrossRef](#)]
16. Yano, R.; Sasagawa, T. Crystal growth and intrinsic properties of $ACrX_2$ ($A = Cu, Ag; X = S, Se$) without a secondary phase. *Cryst. Growth Des.* **2016**, *16*, 5618–5623. [[CrossRef](#)]
17. Naveen, N.; Park, W.B.; Singh, S.P.; Han, S.C.; Ahn, D.; Sohn, K.-S.; Pyo, M. $KCrS_2$ cathode with considerable cyclability and high rate performance: The first K^+ stoichiometric layered compound for potassium-ion batteries. *Adv. Sci. News Nano Micro Small* **2018**, *14*, e1803495. [[CrossRef](#)] [[PubMed](#)]
18. Galuskin, E.; Galuskina, I.O.; Kamenetsky, V.; Vapnik, Y.; Kusz, J.; Zieliński, G. First *in situ* terrestrial osbornite (TiN) in the pyrometamorphic Hatrurim Complex, Israel. *Lithosphere* **2022**, *1*, 8127747. [[CrossRef](#)]
19. Galuskina, I.O.; Galuskin, E.V.; Pakhomova, A.S.; Widmer, R.; Armbruster, T.; Krüger, B.; Grew, E.S.; Vapnik, Y.; Dzierżanowski, P.; Murashko, M. Khesinite, $Ca_4Mg_2Fe^{3+}_{10}O_4[(Fe^{3+}_{10}Si_2)O_{36}]$, a new rhönite-group (sapphirine supergroup) mineral from the Negev Desert, Israel—Natural analogue of the SFCA phase. *Eur. J. Mineral.* **2017**, *29*, 101–116. [[CrossRef](#)]
20. Burg, A.; Kolodny, Y.; Lyakhovskiy, V. Hatrurim-2000: The “Mottled Zone” revisited, forty years later. *Isr. J. Earth Sci.* **1999**, *48*, 209–223.
21. Vapnik, Y.; Sharygin, V.V.; Sokol, E.V.; Shagam, R. Paralavas in a combustion metamorphic complex: Hatrurim Basin, Israel. *Rev. Eng. Geol.* **2007**, *18*, 1–21. [[CrossRef](#)]
22. Novikov, I.; Vapnik, Y.; Safonova, I. Mud volcano origin of the Mottled Zone, South Levant. *Geosci. Front.* **2013**, *4*, 597–619. [[CrossRef](#)]
23. Britvin, S.N.; Murashko, M.N.; Vapnik, Y.; Vlasenko, N.S.; Krzhizhanovskaya, M.G.; Vereshchagin, O.S.; Bocharov, V.N.; Lozhkin, M.S. Cyclophosphates, a new class of native phosphorus compounds, and some insights into prebiotic phosphorylation on early Earth. *Geology* **2020**, *49*, 382–386. [[CrossRef](#)]
24. Sokol, E.; Novikov, I.; Zateeva, S.; Vapnik, Y.; Shagam, R.; Kozmenko, O. Combustion metamorphism in the Nabi Musa dome: New implications for a mud volcanic origin of the Mottled Zone, Dead Sea area. *Basin Res.* **2010**, *22*, 414–438. [[CrossRef](#)]
25. Unger, W.K.; Karecki, D.; Clayman, B.P.; Irwin, J.C. Raman and far-infrared spectra of $NaCrS_2$. *Solid State Commun.* **1979**, *29*, 149–151. [[CrossRef](#)]
26. Caxcer, R.L.; Bricker, C. The Raman spectra of crystalline Na_2CrO , and $Na_2CrO_4 \cdot 4H_2O$. *Spectrochim. Acta Part A Mol. Spectrosc.* **1974**, *30A*, 1793–1800. [[CrossRef](#)]
27. Hardcastle, F.D.; Israel, E.; Wachs, I.E. Raman spectroscopy of chromium oxide supported on Al_2O_3 , TiO_2 and SiO_2 : A comparative study. *J. Mol. Catal.* **1988**, *46*, 173–186. [[CrossRef](#)]
28. Monico, L.; Janssens, K.; Hendriks, E.; Brunetti, B.G.; Miliani, C. Raman study of different crystalline forms of $PbCrO_4$ and $PbCr_{1-x}S_xO_4$ solid solutions for the noninvasive identification of chrome yellows in paintings: A focus on works by Vincent van Gogh. *J. Raman Spectrosc.* **2014**, *45*, 1034–1045. [[CrossRef](#)]
29. Baonza, V.G.; Lobato, A.; Recio, J.M.; Taravillo, M. Charge analysis in (RE)CrO₄ scheelites by combined Raman spectroscopy and computer simulations. *J. Solid State Chem.* **2022**, *316*, 123624. [[CrossRef](#)]
30. Abramova, G.M.; Petrakovskiy, G.A.; Vtyurin, A.N.; Rasch, J.C.E.; Krylov, A.S.; Gerasimova, J.V.; Velikanov, D.A.; Boehmb, V.M.; Sokolov, V. Anomalous Raman phenomenon of $CuCrS_2$. *J. Raman Spectrosc.* **2010**, *41*, 1485–1488. [[CrossRef](#)]
31. Selivanova, A.V.; Sokolov, V.V.; Kolesov, B.A. Raman spectral study of $CuCrS_2$ crystals in the temperature range of 5–300 K. *J. Struct. Chem.* **2015**, *56*, 874–879. [[CrossRef](#)]
32. Gao, W.; Zou, Y.; Zhang, S.; Shi, S.; Xia, Z.; Ouyang, Z.; Liu, B.; Zhang, L.; Li, R.; Pi, L.; et al. Investigation of spin-phonon coupling in triangular-lattice antiferromagnet $AgCrS_2$ by infrared transmission spectroscopy. *J. Magn. Magn. Mater.* **2016**, *404*, 175–178. [[CrossRef](#)]
33. Peng, J.; Liu, Y.; Lv, H.; Li, Y.; Lin, Y.; Su, Y.; Wu, J.; Liu, H.; Guo, Y.; Zhuo, Z.; et al. Stoichiometric two-dimensional non-van der Waals $AgCrS_2$ with superionic behaviour at room temperature. *Nat. Chem.* **2021**, *13*, 1235–1240. [[CrossRef](#)] [[PubMed](#)]
34. Nims, C.; Cron, B.; Wetherington, M.; Macalady, J.; Cosmidis, J. Low frequency Raman Spectroscopy for micron-scale and *in vivo* characterization of elemental sulfur in microbial samples. *Sci. Rep.* **2019**, *9*, 7971. [[CrossRef](#)] [[PubMed](#)]
35. Wang, T.; Ren, G.-X.; Shadike, Z.; Yue, J.-L.; Cao, M.-H.; Zhang, J.-N.; Chen, M.-V.; Yang, X.-Q.; Bak, S.-M.; Northrup, P.; et al. Anionic redox reaction in layered $NaCr_{2/3}Ti_{1/3}S_2$ through electron holes formation and dimerization of S–S. *Nat. Commun.* **2019**, *10*, 4458. [[CrossRef](#)] [[PubMed](#)]
36. Baran, E.J.; Ferrer, E.G.; Bueno, I.; Parada, C. Vibrational spectra of some double chromates the type $LnK(CrO_4)_2$. *J. Raman Spectrosc.* **1990**, *21*, 27–30. [[CrossRef](#)]
37. Frost, R.L. Raman microscopy of selected chromate minerals. *J. Raman Spectrosc.* **2004**, *35*, 153–158. [[CrossRef](#)]
38. Himcinschi, C.; Drechsler, F.; Walch, D.S.; Bhatnagar, A.; Belik, A.A.; Kortus, J. Unexpected phonon behavior in $BiFe_xCr_{1-x}O_3$, a material system different from its $BiFeO_3$ and $BiCrO_3$ parents. *Nanomaterials* **2022**, *12*, 1607. [[CrossRef](#)]
39. Britvin, S.N.; Murashko, M.N.; Vapnik, Y.; Polekhovskiy, Y.S.; Krivovichev, S.V. Earth’s phosphides in Levant and insights into the source of Archean prebiotic phosphorus. *Sci. Rep.* **2015**, *5*, 8355. [[CrossRef](#)]
40. Galuskin, E.V.; Krüger, B.; Galuskina, I.O.; Krüger, H.; Vapnik, Y.; Wojdyla, J.A.; Murashko, M. New mineral with modular structure derived from hatrurite from the pyrometamorphic rocks of the Hatrurim Complex: Ariegilatite, $BaCa_{12}(SiO_4)_4(PO_4)_2F_2O$, from Negev Desert, Israel. *Minerals* **2018**, *8*, 109. [[CrossRef](#)]
41. Griffin, W.L.; Gain, S.E.M.; Saunders, M.; Alard, O.; Shaw, J.; Toledo, V.; O’Reilly, S.Y. Nitrogen under super-reducing conditions: Ti oxynitride melts in xenolithic corundum aggregates from Mt Carmel (N. Israel). *Minerals* **2021**, *11*, 780. [[CrossRef](#)]

42. Anzures, B.A.; Parman, S.W.; Milliken, R.E.; Namur, O.; Cartier, C.; Wang, S. Effect of sulfur speciation on chemical and physical properties of very reduced mercurian melts. *Geochim. Cosmochim. Acta* **2020**, *286*, 780. [[CrossRef](#)]
43. Scheel, H.J. Crystallization of sulfides from alkali polysulfide fluxes. *J. Cryst. Growth* **1974**, *24–25*, 669–673. [[CrossRef](#)]
44. Engelsman, F.M.R.; Wiegers, G.A.; Jellinek, F.; Van Laar, B. Crystal structures and magnetic structures of some metal(I) chromium(III) sulfides and selenides. *J. Solid State Chem.* **1973**, *6*, 574–582. [[CrossRef](#)]
45. Tewari, G.C.; Tripathi, T.S.; Rastogi, A.K. Effect of chromium disorder on the thermoelectric properties of layered-antiferromagnet CuCrS_2 . *Z. Für Krist.* **2010**, *225*, 471–474. [[CrossRef](#)]
46. Shadike, Z.; Zhou, Y.-N.; Chen, L.-L.; Wu, Q.; Yue, J.-L.; Zhang, N.; Yang, X.-Q.; Gu, L.; Liu, X.-S.; Shi, S.-Q.; et al. Antisite occupation induced single anionic redox chemistry and structural stabilization of layered sodium chromium sulfide. *Nat. Commun.* **2017**, *8*, 566. [[CrossRef](#)]
47. Korotaev, E.V.; Syrovashin, M.M.; Filatova, I.Y.; Sotnikov, A.V. Effect of the order-disorder transition on the electronic structure and physical properties of layered CuCrS_2 . *Materials* **2021**, *14*, 2729. [[CrossRef](#)]
48. Xu, X.; Zhong, T.; Zuo, N.; Li, Z.; Li, D.; Pi, L.; Chen, P.; Wu, M.; Zhai, T.; Zhou, X. High-TC two-dimensional ferroelectric CuCrS_2 grown via chemical vapor deposition. *Am. Chem. Soc. Nano* **2022**, *16*, 8141–8149. [[CrossRef](#)]
49. Schöllhorn, R.; Ardnt, R.; Kubny, A. Formation and reactions of hydrated layered chromium sulfides $A_x(\text{H}_2\text{O})_y[\text{CrS}_2]$. *J. Solid State Chem.* **1979**, *29*, 259–265. [[CrossRef](#)]

Disclaimer/Publisher’s Note: The statements, opinions and data contained in all publications are solely those of the individual author(s) and contributor(s) and not of MDPI and/or the editor(s). MDPI and/or the editor(s) disclaim responsibility for any injury to people or property resulting from any ideas, methods, instructions or products referred to in the content.